Front. Chem. Sci. Eng. 2023, 17(6): 691−703
https://doi.org/10.1007/s11705-022-2268-6

RESEARCH ARTICLE

Construction of $NiCo_2O_4$ nanoflake arrays on cellulose-derived carbon nanofibers as a freestanding electrode for high-performance supercapacitors

Xuepeng Ni[1], Kunming Li[1], Changlei Li[3], Qianqian Wu[1], Chenglin Liu[1], Huifang Chen[1,2], Qilin Wu[1,2], Anqi Ju (✉)[1,2]

1 College of Materials Science and Engineering & State Key Laboratory for Modification of Chemical Fibers and Polymer Materials, Donghua University, Shanghai 201620, China
2 Key Laboratory of High-Performance Fibers & Products, Ministry of Education, Donghua University, Shanghai 201620, China
3 Weifang Xinlong Biomaterial Co., Ltd., Weifang 261000, China

Abstract Cellulose has a wide range of applications in many fields due to their naturally degradable and low-cost characteristics, but few studies can achieve cellulose-nanofibers by conventional electrospinning. Herein, we demonstrate that the freestanding cellulose-based carbon nanofibers are successfully obtained by a special design of electrospinning firstly, pre-oxidation and high-temperature carbonization (1600 °C), which display a superior electrical conductivity of 31.2 $S\cdot cm^{-1}$ and larger specific surface area of 35.61 $m^2\cdot g^{-1}$ than that of the polyacrylonitrile-based carbon nanofibers (electrical conductivity of 18.5 $S\cdot cm^{-1}$, specific surface area of 12 $m^2\cdot g^{-1}$). The $NiCo_2O_4$ nanoflake arrays are grown uniformly on the cellulose-based carbon nanofibers successfully by a facile one-step solvothermal and calcination method. The as-prepared cellulose-based carbon nanofibers/$NiCo_2O_4$ nanoflake arrays are directly used as electrodes to achieve a high specific capacitance of 1010 $F\cdot g^{-1}$ at 1 $A\cdot g^{-1}$ and a good cycling stability with 90.84% capacitance retention after 3000 times at 10 $A\cdot g^{-1}$. Furthermore, the all-solid-state symmetric supercapacitors assembled from the cellulose-based carbon nanofibers/$NiCo_2O_4$ deliver a high energy density of 62 $W\cdot h\cdot kg^{-1}$ at a power density of 1200 $W\cdot kg^{-1}$. Six all-solid-state symmetric supercapacitors in series can also power a 'DHU' logo consisted of 36 light emitting diodes, confirming that the cellulose-based carbon nanofiber is a promising carbon matrix material for energy storage devices.

Keywords cellulose, carbon nanofibers, $NiCo_2O_4$, supercapacitors

Received July 18, 2022; accepted October 1, 2022

E-mail: anqiju@163.com

1 Introduction

Currently, it is urgent to demand for portable, safe, renewable, eco-friendly energy storage devices due to the limited fossil fuel supply and serious environmental pollution. Supercapacitors have drew much attention because of their high power density, superb cycling stability and short charging time [1]. There are mainly two energy storage mechanisms in supercapacitors: electrical double layers and pseudo-capacitance [2]. The composition, structure and specific surface area of electrode materials have a great effect in electrochemical performance of supercapacitors [1,3–5]. Up to now, many kinds of electrode materials, such as carbon materials [6,7] and transition metal oxides [8,9], sulfides [10,11], hydroxides [12,13] as well as their combination [14–16] have been widely studied. Especially, composites of carbon materials and binary transition metal oxide were extensively used in high energy density supercapacitors, because carbon materials can not only improve the electrical conductivity, but also buffer the volume expansion of transition metal materials during the cycling.

Carbon materials, including MXene, carbon foam, graphene, carbon nanotubes, micro/meso-porous carbon sphere and carbon nanofibers (CNFs) have been reported a lot. Among them, CNFs have attracted the most attention due to large surface area, light-weight as well as unique three-dimensional (3D) networks, which are directly used as current collector without binders and conductive additives. Most of the carbon fiber precursors are petrochemicals, such as polyacrylonitrile, polyvinylpyrrolidone, polybenzimidazole and pitch, which are high-cost products and emit toxic gases during carbonization.

However, cellulose is a better precursor for CNFs because it is low-cost, renewable and natural abundant. There are few reports that the cellulosic derivatives (cellulose acetate and methyl cellulose) nanofibers can be prepared by conventional electrospinning [17–19], but the cellulosic derivatives-based carbon fibers are fragile and the carbon yield is low. It is still a difficult task to obtain freestanding cellulose-based CNFs (C-CNFs) with a unique interconnected fiber network structure owing to the fact that the cellulose is a macromolecular polysaccharide composed of glucose with a specific molecular structure. Additionally, the α-cellulose cannot be dissolved into the water, but only in a few organic solvents due to the rigid pyranose ring structure, and its trifluoroacetic acid/methylene dichloride solution has low viscosity. Therefore, it is difficult for α-cellulose to be used in electrospinning by itself. However, the addition of polyethylene oxide (PEO) can effectively reduce surface tension of electrospinning precursor solution, aiding in fiber formation. In this work, the cellulose nanofibers (C-NFs) were successfully prepared through a special design of new electrospinning receiver with PEO as additives in this study. Then, the freestanding interconnected C-CNFs were successfully obtained after pre-oxidation and carbonization. Although the C-CNFs have been used as freestanding electrodes, the lower capacity cannot meet the requirements of energy storage devices. Thus, the freestanding C-CNFs substrates should be loaded with active materials to directly served as binder-free electrodes for high-performance supercapacitors.

A variety of active electrode materials with high specific capacitance, especially pseudo-capacitive materials (transition metal oxides/sulfides) embrace ultrahigh theoretical capacitance and excellent electrochemical activity. Among them, $NiCo_2O_4$, a binary transition metal oxide, is extensively researched as electrodes for supercapacitors because of the high theoretical capacity (1370 $F\cdot g^{-1}$), rich valence state and lower activation energy for ion and electron transport [18,20–22]. However, the single $NiCo_2O_4$ usually suffers from a serious structural distortion during the charge/discharge storage process because of the low electrical conductivity and poor mechanical/chemical stability, which reduces the energy storage capability and restricts it application in supercapacitors [23,24]. To enhance the electrochemical property of $NiCo_2O_4$, it is an effective strategy to use the as-prepared C-CNFs as freestanding carbon substrates to support $NiCo_2O_4$. As a result, the $NiCo_2O_4$ nanoflake arrays are uniformly coated on C-CNFs by one-step solvothermal method to obtain binder-free C-CNFs/$NiCo_2O_4$ nanoflake arrays. Benefiting from the 3D interconnected network structure, the formed C-CNFs/$NiCo_2O_4$ composite can obtain superior electrochemical performance, such as a higher specific capacitance (1010 $F\cdot g^{-1}$ at 1 $A\cdot g^{-1}$) and better cycling stability (90.84% capacitance retention at 10 $A\cdot g^{-1}$ after 3000 times). Moreover, the all-solid-state symmetric supercapacitors (ASSCs) constructed with C-CNFs/$NiCo_2O_4$ can power the 'DHU' logo consisting of 36 light emitting diodes (LEDs) and thus exhibiting a huge potential of the C-CNFs as carbon matrix in energy storage devices.

2 Experimental

2.1 Preparation of C-CNFs

All regents were analytical grade which could be used directly in the present study. Both α-cellulose and PEO (9:1 w/w) were added into a mixed solution of trifluoroacetic acid and methylene dichloride (9:1 w/w) at room temperature by stirring for 72 h until complete dissolution. The α-cellulose/PEO solution with various concentration (3.5–7.0 wt %) was transferred into a 5 mL syringe with a steel needle to be electrospun. It was 13 cm between the needle tip and the collector. The flow rate was 0.75 $mL\cdot h^{-1}$ using a syringe pump (LSP01-3A, Longer Pump), the applied positive voltage was 17 kV and applied negative voltage was 3.0 kV. The C-NFs were gathered by the modified new electrospinning receiving devices. Afterwards, the C-NFs were pre-oxidized at 245 °C for 90 min in air and carbonized at 1600 °C at a rate of 10 $°C\cdot min^{-1}$ under N_2 atmosphere for 30 min to obtain C-CNFs. The thickness and areal specific mass of C-CNFs were ~0.08 mm and 1.5 $g\cdot cm^{-2}$, respectively. To explore the effect of carbonization temperature on the properties of C-CNFs, the carbonization temperature of C-NFs was added to 800 and 1200 °C, respectively. For comparison, the CNFs based on poly(acrylonitrile-*co*-methylhydrogen itaconate) (P-CNFs) were also prepared in our previous work [25].

2.2 Synthesis of C-CNFs/$NiCo_2O_4$ nanoflake arrays

The C-CNFs/$NiCo_2O_4$ composite was synthesized via a facile solvothermal method. In detail, 0.1 g $Ni(NO_3)_2\cdot 6H_2O$, 0.2 g $Co(NO_3)_2\cdot 6H_2O$ and 0.3 g hexamethylenetetramine were dissolved in 48 mL methanol with stirring for 10 min and then transferred into a 50 mL Teflon-lined stainless steel autoclave. A piece of C-CNFs (2 cm × 4 cm) was immersed into the solution vertically, and heated to 150 °C for 8 h. When the reaction was completed and cooled to room temperature, the C-CNFs/$NiCo_2O_4$ precursor was taken out and washed multiple times by deionized water and alcohol, then dried at 60 °C overnight in an oven. At last, C-CNFs/$NiCo_2O_4$ nanoflake arrays were obtained by annealing the precursor at 350 °C for 2 h with heating rate of 2 $°C\cdot min^{-1}$. For comparison, P-CNFs/$NiCo_2O_4$ nanoflake arrays were synthesized by using P-CNFs instead of C-CNFs with a similar procedure of C-CNFs/$NiCo_2O_4$ nanoflake arrays.

2.3 Materials characterization

The microstructure of the samples was characterized by field emission scanning electron microscope (SEM, Hitachi SU8010, Japan) and high-resolution transmission electron microscopy (HRTEM, FEI Talos F200S, USA). The crystal structure of the samples was analyzed by an X-ray diffraction diffractometer (XRD, Rigaku D/max-2550, Cu Kα, scan rate: 2 °·min^{-1}). X-ray photoelectron spectroscopy (XPS, Escalab-250Xi) was employed to obtain the surface elements composition of the sample and binding energy of elements. The structure of electrodes was measured by Raman spectrometer (inVia Reflex, 633 nm, China). The content of $NiCo_2O_4$ in the composites was obtained by thermogravimetric analysis (TGA, 209 F1). The Fourier transform infrared (FTIR) spectra of samples were characterized by using the NEXUS-670 spectrometer. The nitrogen adsorption–desorption isotherms and pore size distribution of the electrodes were achieved by a fully automatic specific surface area and pore size tester (ASAP2460) at 77 K. The C element was determined by the elemental analyzer (VarioEL-III, Germany) and the electrical conductivities of both C-CNFs and P-CNFs were measured using a four-point probe (MCP-T370, China).

2.4 Electrochemical measurements

Electrochemical characterization of the samples was carried out by an electrochemical workstation (Ivium-V01320). The three-electrode cell was composed of reference electrode (saturated calomel electrode), counter electrode (Pt plate) and working electrode, and the electrolyte was 2 mol·L^{-1} KOH aqueous, which was used for cyclic voltammetry (CV), galvanostatic charge-discharge (GCD), and electrochemical impedance spectroscopy (EIS). The CV curves were performed in the range of 5–80 mV·s^{-1} at a potential window of –0.1–0.6 V. The current densities of GCD were in the range from 1 to 10 A·g^{-1} at the potential range of 0 to 0.45 V. The EIS measurements were performed at an open circuit potential in the frequency range of 0.01 Hz to 100 kHz. The specific capacitance was calculated by the following formula:

$$C = \frac{I\Delta t}{m\Delta V}. \tag{1}$$

Therein, C (F·g^{-1}) represents the specific capacitance, the I (A) represents charge or discharge current, m (g) is the mass of active materials, ΔV (V) designates the voltage window.

2.5 Preparation of ASSCs

Polyvinyl alcohol (PVA) (3 g) and KOH (0.6 g) were dissolved in the deionized water (40 mL) under 85 °C to obtain PVA-KOH gel electrolyte. Two pieces of electrodes (C-CNFs/$NiCo_2O_4$, 1 cm × 2.5 cm) and a piece of polyethylene (PE, 2 cm × 4 cm) were put in the gel electrolyte immersing for 10 min and dried at room temperature. Then, the two pieces of electrodes with PE as the separator were assembled to fabricate the ASSC, which was on the PE terephthalate substrate.

In the two-electrode systems, the specific energy density (W·h·kg^{-1}) and specific power density (W·kg^{-1}) of the assembled ASSCs were calculated according to the Eqs. (2), (3) and (4), respectively.

$$C = \frac{I\Delta t}{2m\Delta V}, \tag{2}$$

$$E = \frac{C\Delta V^2}{2\times 3.6}, \tag{3}$$

$$P = \frac{3600E}{\Delta t}, \tag{4}$$

where E (W·h·kg^{-1}) is energy density, C (F·g^{-1}) is specific capacitance, ΔV (V) is the potential range, P (W·kg^{-1}) is the power density, and Δt (s) is the discharge time.

3 Results and discussion

3.1 Materials characterization

Scheme 1(a) shows the preparation process of C-NFs, the positive voltage is attached to the syringe needle and electrospinning receiver is applied negative voltage. It could be seen that the receiving device is covered by a thick and uniform C-NFs film. As from Scheme 1(b), the C-CNFs were acquired after stabilization in air and carbonization in N_2, and the as-prepared C-CNFs were immersed into mixed solutions by solvothermal reaction to obtain C-CNFs/$NiCo_2O_4$ precursor. After annealed, the C-CNFs/$NiCo_2O_4$ nanoflake arrays electrodes were successfully fabricated.

The concentration of electrospinning precursor played a significant role in the stable interconnected C-NFs, and was studied by adjusting to the concentration of α-cellulose/PEO, using same syringe (5 mL) and needles (17 G) in the electrospinning process. SEM images display different morphologies of C-NFs with various concentration of electrospinning precursor (Figs. 1 and S1, cf. Electronic Supplementary Material, ESM). The continuous and interconnected C-NFs networks were successfully prepared using 6.0 and 6.5 wt % of electrospinning precursor (Fig. 1(a) and inset, Figs. S1(d) and S1(e)). When the concentrations were reduced to lower values (5.5, 4.5 or 3.5 wt %), the surface of the C-NFs gradually emerged some beads and failed to form the uniform structure (Figs. S1(a–c)). The C-NFs obtained at higher solution concentration (7.0 wt %) were bonded

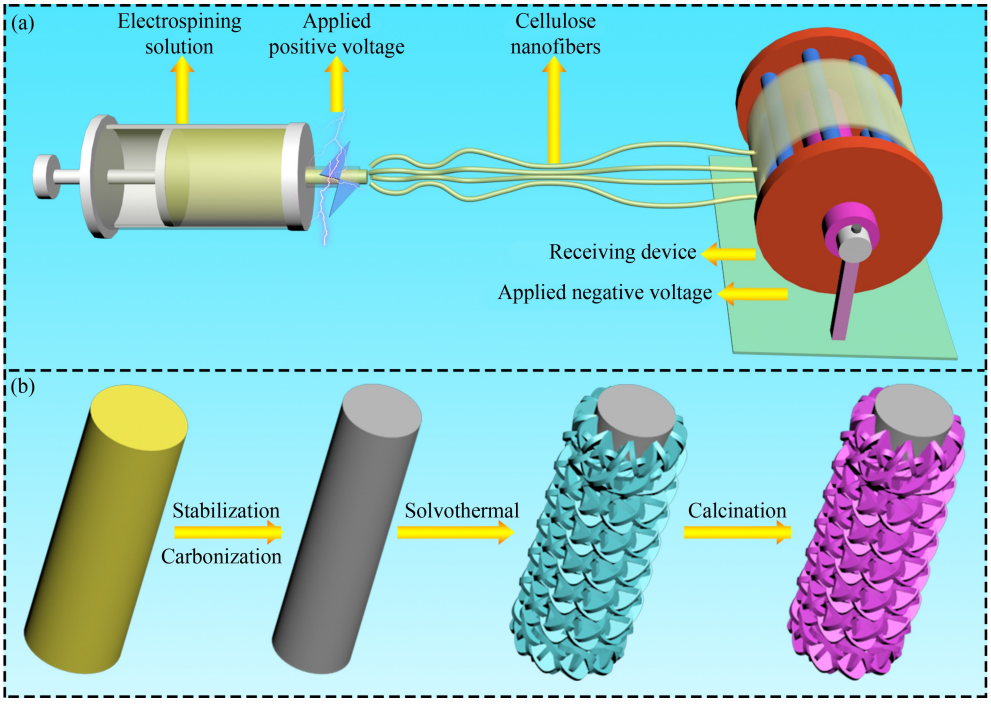

Scheme 1 Schematic illustration of the preparation of C-CNFs/$NiCo_2O_4$ nanoflake arrays.

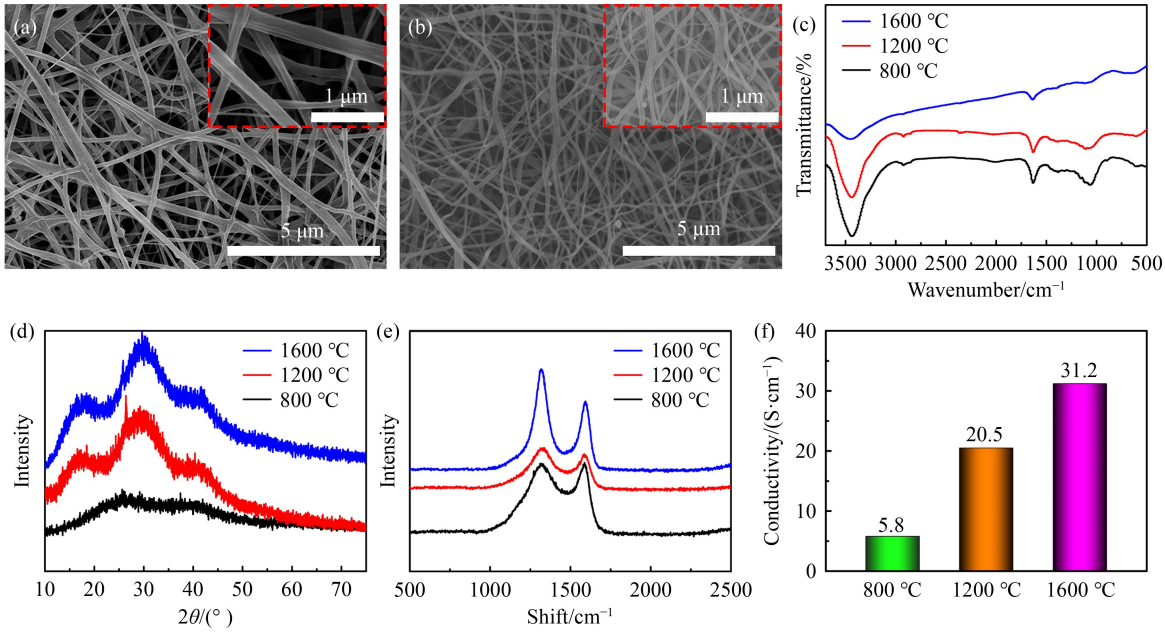

Fig. 1 The SEM images of (a) C-NFs and (b) C-CNFs; the comparison of (c) FTIR spectra, (d) XRD pattern, (e) Raman spectra and (f) electrical conductivity of C-CNFs at different carbonization temperatures. The insets of (a) and (b) are the closer observation under a higher magnification factor.

together, and continuous and interconnected C-NF disappeared (Fig. S1(f)). In addition, Fig. 1(b) and inset revealed that the C-CNFs (α-cellulose/PEO-6.0 wt %) still maintained uniform and interconnected networks after carbonization of C-NFs, which was similar with morphology of C-NFs. However, the C-NF membrane contracted to a large extent, and the diameter of C-CNFs decreased significantly after carbonization of C-NFs (Fig. 1(b) and inset). The results of SEM images exhibited the two cases: (1) the C-NFs without beads failed to form a closely interconnected 3D framework at lower concentration of α-cellulose/PEO; (2) the C-NFs could tangle and form bundles when the concentrations of electrospinning precursor solutions were increased to a high value.

To observe the effect of different carbonization

temperatures on the chemical structure of C-CNFs, the FTIR spectra were displayed in Fig. 1(c). With the carbonization temperature increasing, the intensity of the stretching vibration absorption peak of the –OH (3400 cm^{-1}), the C–H (2900 cm^{-1}) and C=O stretching vibration peak (1061 cm^{-1}) [26,27], gradually weakened or even disappeared, indicating that the more complete the removal of hydrogen and oxygen in the molecular chain with the higher carbonization temperature. The XRD pattern of C-CNFs was employed to explore the structural changes at various carbonization temperatures. From Fig. 1(d), two broad diffraction peaks around 30° and 42.5° belonged to amorphous carbon [28], and the intensity of diffraction peak at 30° would be strong with a higher carbonization temperature, confirming a good crystallinity of C-CNFs at 1600 °C. In addition, the Raman spectra of C-CNFs (Fig. 1(e)) revealed two obvious D (1351 cm^{-1}) of disordered carbon structure and G peaks (1599 cm^{-1}) of graphitic carbon structure, respectively. The degree of graphitization is evaluated via intensity ratio of D to G bands (I_D/I_G), and the value of I_D/I_G also increases from 1.01 to 1.48 with the carbonization temperature from 800 to 1600 °C, which was in keeping with the reported literature [29–31]. Derived from the quantitative elemental contents analyzed by elemental analysis, the carbon contents of C-CNFs were 88.38% (800 °C), 90.74% (1200 °C) and 98.76% (1600 °C), respectively (Table S1, cf. ESM). The electrical conductivities of C-CNFs with different carbonization temperature were characterized by Four-probe Tester, the Fig. 1(f) showed that the C-CNFs carbonized at 1600 °C had a higher conductivity (31.2 $S\cdot cm^{-1}$) than those of other C-CNFs (5.8 $S\cdot cm^{-1}$, 800 °C; 20.5 $S\cdot cm^{-1}$, 1200 °C). Especially, the conductivity of C-CNFs carbonized at 1600 °C was 1.69 times of P-CNFs carbonized at 1600 °C (18.5 $S\cdot cm^{-1}$) (Fig. S2, cf. ESM), further indicating C-CNFs could be used as a potential carbon matrix for electrode materials.

The C-CNFs prepared by 1600 °C were used as carbon substrates to combine with $NiCo_2O_4$ for supercapacitors. The SEM and (HR)TEM images of C-CNFs/$NiCo_2O_4$ nanoflake arrays were illustrated in Fig. 2. The $NiCo_2O_4$ nanoflake arrays uniformly covered with the surface of interconnected C-CNFs, forming highly ordered nanoflake arrays with the thickness of the average diameter of 190 nm (Figs. 2(a) and 2(b) and inset). Apparently, there was no obvious morphology change of C-CNFs/$NiCo_2O_4$ nanoflake arrays before and after calcination. The stability of nanoflake arrays can strengthen the contact area between electrolyte and electrodes, accumulate the penetration rate of ions, and boost the process of redox reaction. For compassion, the SEM images of P-CNFs/$NiCo_2O_4$ nanoflake arrays and bare $NiCo_2O_4$ were shown in Figs. S3 and S4 (cf. ESM), respectively. The morphology of the P-CNFs/$NiCo_2O_4$ nanoflake arrays was similar with C-CNFs/$NiCo_2O_4$ nanoflake arrays, and the ultrathin nanoflake arrays were uniformly grown on the surface of P-CNFs in Figs. S3(a) and S3(b). Obviously, bare $NiCo_2O_4$ was composed of irregular flakes in Figs. S4(a) and S4(b). The TEM images in Fig. 2(d) illustrated as-prepared C-CNFs/$NiCo_2O_4$ nanoflake arrays with the C-CNFs inside (ca. 150 nm) and the ultrathin nanoflake arrays (ca. 190–200 nm) on the surface. The HRTEM image in Fig. 2(e) revealed two obvious lattice fringes with interplane spacing are 0.148 and 0.204 nm, corresponding to the (440) and (400) crystal planes of spinel $NiCo_2O_4$, respectively. The TEM and energy-dispersive X-ray spectroscopy (EDS) mapping is characterized in Figs. 2(c) and 2(f) to show the elements distribution of

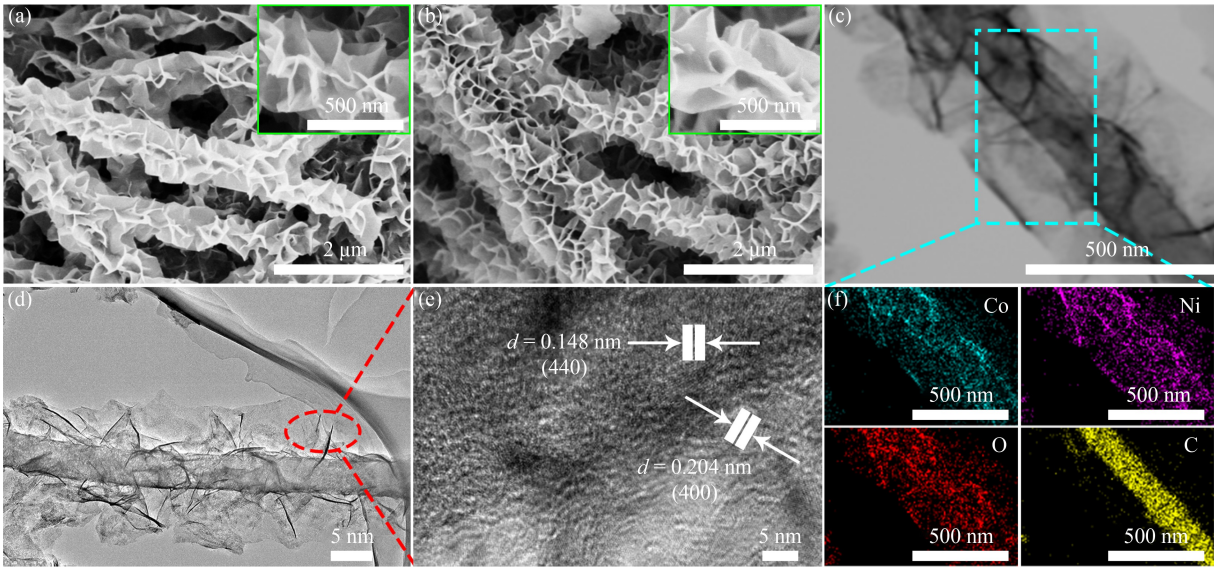

Fig. 2 SEM images of (a) C-CNFs/$NiCo_2O_4$ precursors and inset image is the high magnification of (a) and (b) C-CNFs/$NiCo_2O_4$ nanoflake arrays and inset image is the high magnification of (b) after calcination. (c), (d) TEM images; (e) HRTEM image; (f) elemental mapping (Co, Ni, O and C) of C-CNFs/$NiCo_2O_4$ nanoflake arrays.

Co, Ni, O and C. The C was mainly concentrated in the inner part, corresponding to C-CNFs and the Ni, Co and O are distributed on the outer sides, originating from the surface of $NiCo_2O_4$ nanoflake arrays, which exhibited uniform elements distribution in the C-CNFs/$NiCo_2O_4$ electrode. Additionally, the TEM image and EDS mapping of bare $NiCo_2O_4$ were also illustrated in Figs. S4(c) and S4(d), some thin irregular flakes formed bare $NiCo_2O_4$ and the Ni, Co and O were evenly distributed within the flakes.

The crystal features of the C-CNFs and C-CNFs/$NiCo_2O_4$ electrode were analyzed by XRD in Fig. 3. As shown in Fig. 3(a), a typical crystalline peak at $2\theta = 26°$ for C-CNFs and C-CNFs/$NiCo_2O_4$ nanoflake arrays, which was in accordance with amorphous carbon [28,32]. However, a series of relatively weak diffraction peaks at 2θ values of 31.2, 36.7, 44.6, 59.1 and 65.0 could be ascribed to (220), (311), (400), (511), and (440) plane, respectively, which correspond to standard diffraction peaks of the spinel structure $NiCo_2O_4$ (JCPDS 20-0781). In Fig. 3(b), the Raman spectra clearly illustrated the D (1350 cm^{-1}) of disordered carbon structure and G peaks (1590 cm^{-1}) of graphitic carbon structure for two materials, respectively [4]. The Raman peaks at 192.4, 476.2, 527.2 and 652.7 cm^{-1} were in good agreement with the F_{2g}, E_g, F_{2g} and A_{1g} vibration modes of Ni–O and Co–O in $NiCo_2O_4$, respectively. These results were consistent with the results of XRD analysis.

The N_2 adsorption–desorption isotherms and the pore size distribution curves were analyzed in Figs. 3(c) and S(5–7) (cf. ESM). The N_2 adsorption–desorption isotherms revealed a typical type IV isotherm with H2-H3 hysteresis loops, confirming that the mesoporous structure of all the as-prepared materials. For carbon matrix comparison, according to the above analysis results, Fig. S5 illustrated the Brunner–Emmett–Teller specific surface area of C-CNFs was 35.61 $m^2 \cdot g^{-1}$, larger than the P-CNFs (12.0 $m^2 \cdot g^{-1}$), indicating that C-CNFs were more suitable as carbon substrate material to combine with $NiCo_2O_4$. In addition, the specific surface area (85.61 $m^2 \cdot g^{-1}$) of C-CNFs/$NiCo_2O_4$ nanoflake arrays was 2.86 times that of P-CNFs/$NiCo_2O_4$ nanoflake arrays (29.98 $m^2 \cdot g^{-1}$ in Fig. S6). From the inset of Fig. 3(c), the mesopore size distribution of C-CNFs/$NiCo_2O_4$ nanoflake arrays mainly concentrated at 3.6 nm, and the main mesopore diameter of P-CNFs/$NiCo_2O_4$ nanoflake arrays was about 2 nm. Additionally, for the bare $NiCo_2O_4$ in Fig. S7, the specific surface area was only 18.7 $m^2 \cdot g^{-1}$, which was much lower than that of C-CNFs/$NiCo_2O_4$ nanoflake arrays. And the mesopore diameter of bare $NiCo_2O_4$ primarily lied at 2.6 nm. The interconnected meso-porosity of C-CNFs/$NiCo_2O_4$ nanoflake arrays with higher specific surface area could buffer the volume change and offer more diffusion channels for the fast ion

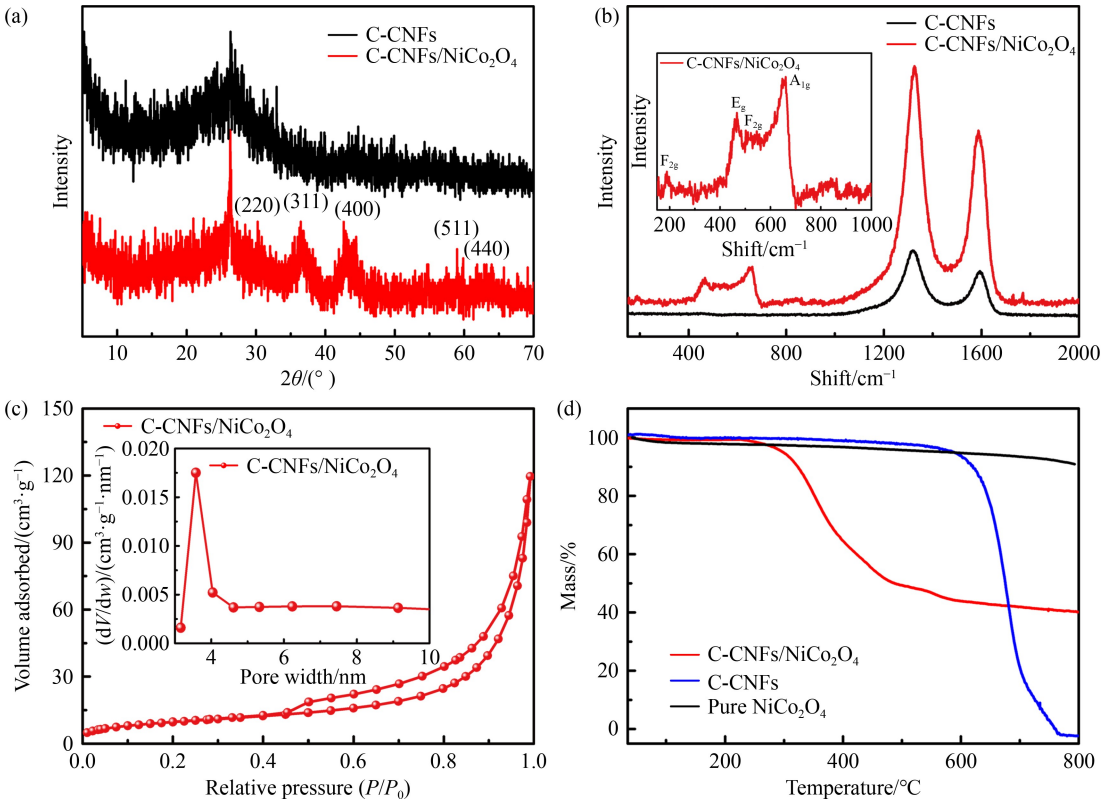

Fig. 3 (a) XRD patterns and (b) Raman spectrums of C-CNFs and C-CNFs/$NiCo_2O_4$ nanoflake arrays; (c) N_2 adsorption–desorption isotherms and pore size distribution curves of C-CNFs/$NiCo_2O_4$ nanoflake arrays; (d) TG patterns of C-CNFs/$NiCo_2O_4$ nanoflake arrays, C-CNFs and pure $NiCo_2O_4$.

transfer during charge/discharge. The contents of $NiCo_2O_4$ and carbon were calculated by TG curves under air condition (Figs. 3(d) and S8, cf. ESM). And the contents of $NiCo_2O_4$ in C-CNFs/$NiCo_2O_4$ and P-CNFs/$NiCo_2O_4$ nanoflake arrays were 44.8% and 38.6%, respectively. The content of $NiCo_2O_4$ in C-CNFs/$NiCo_2O_4$ confirmed that C-CNFs were beneficial to improve the mass loading of active materials and increase the specific capacitance of supercapacitors.

To further analyze the atomic composition and binding energy of C-CNFs/$NiCo_2O_4$ electrode materials, the XPS spectra was measured in Fig. 4. The full XPS survey scan spectra (Fig. 4(a)) revealed the existence of Ni, Co, O and C, which was in accordance with the TEM mapping. The high-resolution spectrum of Ni 2p was displayed in Fig. 4(b), peaks at 873.3 and 855.8 eV were attributed to the Ni^{3+}, while the ones at 871.7 and 853.9 eV were assigned to Ni^{2+} [33]. Two obvious shakeup satellite peaks were located at 872.3 and 855.1 eV. For the Co 2p high-resolution spectrum (Fig. 4(c)), there were two doublet peaks for fitting peaks at 796.8 and 781.5 eV, which corresponded to the Co^{2+}, and the peaks at 795.3 and 779.4 eV are indexed to Co^{3+} [21]. And the peaks located at 802.9 and 785.7 eV were ascribed to satellite peaks. The O 1s spectra in Fig. 4(d) had three characteristic peaks, the binding energies of 529.2, 530.6 and 531.4 eV were assigned to the characteristic peaks of the metal–oxygen bond M–O–M (M = Ni or Co, O_1), the defects with low oxygen coordination in materials (O_2) and the oxygen in the hydroxyl groups within the surface of materials (O_3), respectively [20,34]. In addition, there were also three fitted peaks in the spectrum of C 1s (Fig. S9, cf. ESM), C=C–C (284.0 eV), C–O (284.7 eV) and O–C=O (287.7 eV). The results confirmed that the elements of Ni and Co possessed rich valence states (Ni^{2+}/$Ni^{3+}$and Co^{2+}/Co^{3+}), which might be conducive to enhance the electrochemical performance of supercapacitors.

3.2 Electrochemical performance

The CV measurements of C-CNFs/$NiCo_2O_4$ and P-CNFs/$NiCo_2O_4$ nanoflake arrays were tested in a three-electrodes using 2 $mol \cdot L^{-1}$ KOH aqueous electrodes at a potential window of –0.1–0.6 V from 5 to 50 $mV \cdot s^{-1}$ in Figs. 5(a) and S10 (cf. ESM). As illustrated in Figs. 5(a) and S10, a pair of well-defined redox peaks within –0.1 to 0.6 V can be clearly observed, which is mainly ascribed to the faradaic reactions. And the shape of CV curves maintained unchanged and the peaks of CV kept similar position with the scanning rates increasing, indicating the rapid redox reactions and good reversibility due to the 3D fiber networks facilitating the fast transfer of electron [4,35,36]. In addition, the integrated area of the CV curves (C-CNFs/$NiCo_2O_4$) was higher that of the P-CNFs/$NiCo_2O_4$ at 5 $mV \cdot s^{-1}$, which showed the C-CNFs/$NiCo_2O_4$ possessed a specific capacitance. The reason may be that higher contact surface between electrodes and electrolytes, providing more active sites owing to the larger

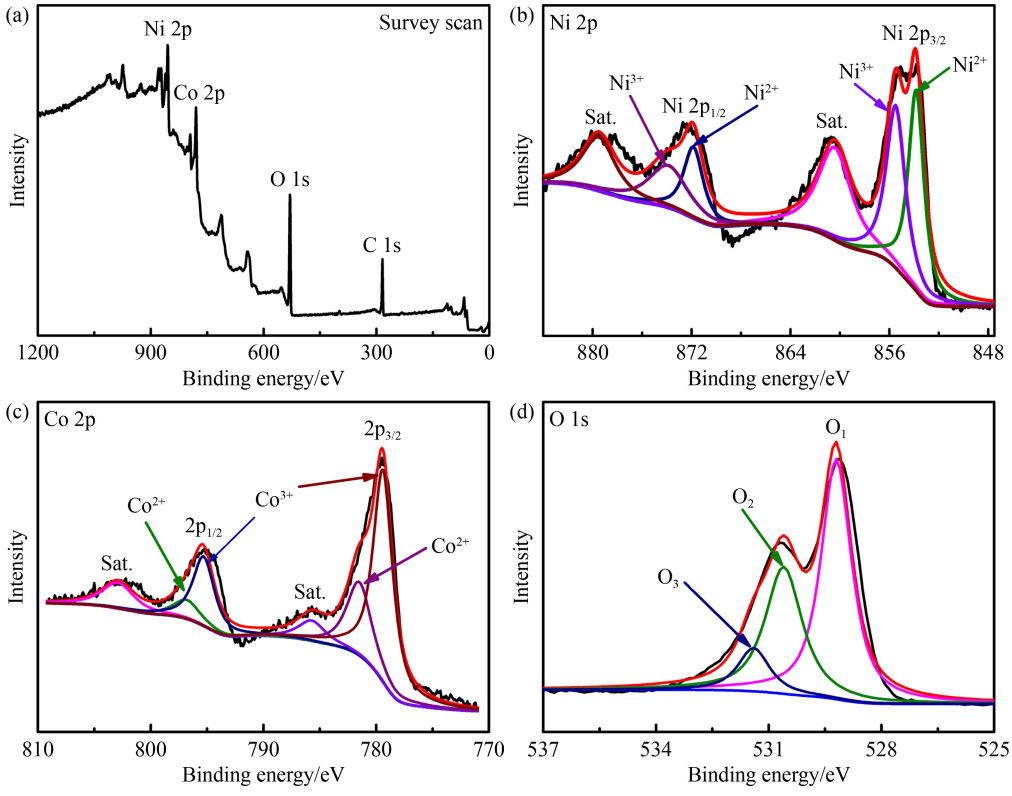

Fig. 4 XPS spectra of C-CNFs/$NiCo_2O_4$ nanoflake arrays: (a) the survey scan, (b) Ni 2p, (c) Co 2p, (d) O 1s.

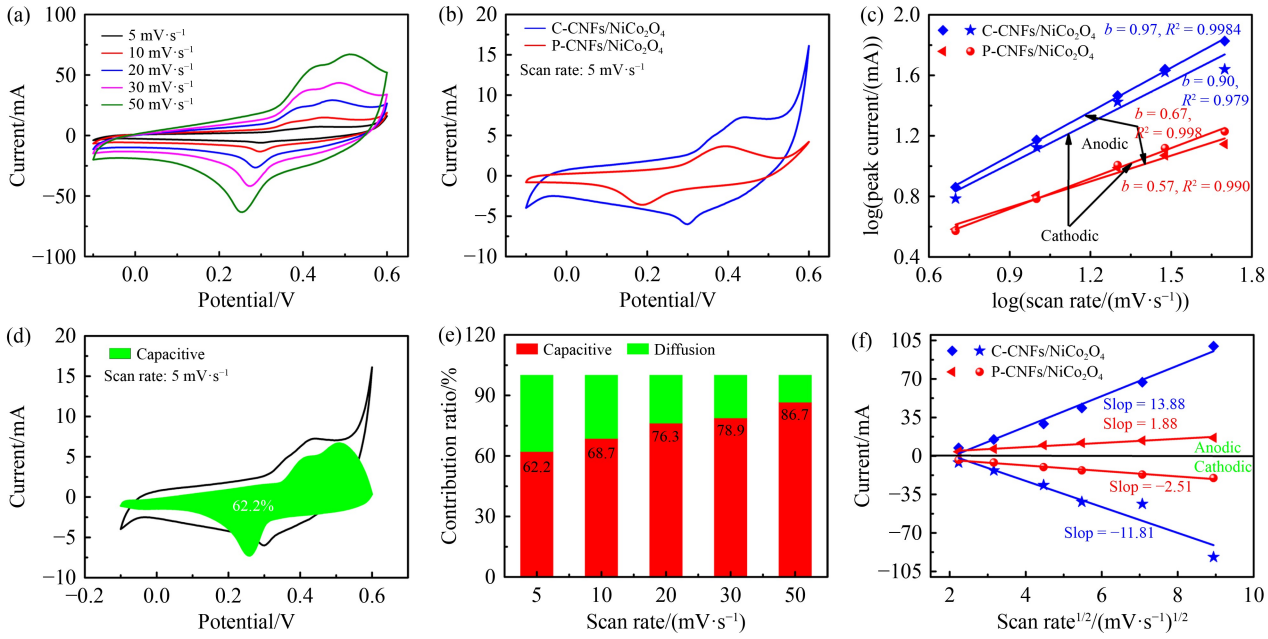

Fig. 5 (a) The CV curves of C-CNFs/$NiCo_2O_4$ nanoflake arrays at various scan rates. (b) The comparison of CV curves at 5 mV·s^{-1} and (c) logarithm relationship between anodic/cathodic peaks current and scan rate of C-CNFs/$NiCo_2O_4$ and P-CNFs/$NiCo_2O_4$ nanoflake arrays. (d) The capacitive contribution at 5 mV·s^{-1} and (e) contribution comparison at different scan rates of C-CNFs/$NiCo_2O_4$ nanoflake arrays. (f) Linear relationship of the anodic/cathodic peaks current (i_p) and the square root of the scan rate ($v^{1/2}$) for C-CNFs/$NiCo_2O_4$ and P-CNFs/$NiCo_2O_4$ nanoflake arrays.

specific surface area of C-CNFs/$NiCo_2O_4$ (Fig. 5(b)). And the peaks at 0.3 and 0.43 V were in keep with the revisable reactions of Co^{3+}/Co^{4+} and Ni^{2+}/Ni^{3+} [36]. The redox reactions were described by the following equations [4,37]:

$$NiCo_2O_4 + OH^- + H_2O = NiOOH + 2CoOOH + e^- \quad (5)$$

$$2CoOOH + OH^- = 2CoO_2 + H_2O + e^- \quad (6)$$

To further analyze the electrochemical kinetics of electrode materials. The relationship between the redox peaks current (i) and various scan rates (v) was measured by the following formula [38]:

$$i = av^b \rightrightarrows \log i = \log a + b\log v. \quad (7)$$

Here the values of a and b were constants. The b value is between 0.5 and 1, which was calculated by the slop of log$i$ versus log$v$ plot. As we all know, the value of b approaches 0.5, indicating the diffusion-controlled process. And the b value is closed to 1, which reveals the capacitance-controlled mechanism. Figure 5(c) depicted that the calculated b values of C-CNFs/$NiCo_2O_4$ nanoflake arrays for anodic and cathodic peaks were 0.97 and 0.90, which were higher than that of 0.57 (anodic peak) and 0.67 (cathodic peak) for P-CNFs/$NiCo_2O_4$ nanoflake arrays, respectively. And the total capacitances of C-CNFs/$NiCo_2O_4$ electrode were predominant by the capacitive-controlled reactions, revealing that the ultrathin nanoflake arrays and C-CNFs allowed penetration ions of electrolytes more easily, accumulating fast kinetics process of ions transfers, which contributed to the charge/discharge process at high current densities.

Moreover, to obtain the ratios of capacitive contribution in the total capacitance, the current response $i(V)$ at constant potential was divided into capacitance-controlled effects (k_1v) and diffusion-dominated process ($k_2v^{1/2}$) based on the following equation:

$$i(V) = k_1v + k_2v^{1/2} \rightrightarrows i(V)/v^{1/2} = k_1v^{1/2} + k_2, \quad (8)$$

where $i(V)$ and v were current at constant potential and scan rates, respectively. And the values of k_1 and k_2 could be calculated by the slop and intercept of the $i(V)/v^{1/2}$ vs. $v^{1/2}$ plot, respectively. By fitting the CV curves at various sweep rates at a fixed potential, the contribution of the capacitance-controlled to the entire current can be obtained. Figure 5(d) exhibited the capacitive contribution of C-CNFs/$NiCo_2O_4$ nanoflake arrays accounted for 62.2% at 5 mV·s^{-1}, confirming that the electrochemical reaction was indeed controlled by the capacitive process. To compare the changes in capacitive contribution at various scan rates, Figs. 5(e) and S11 (cf. ESM) revealed capacitive process at higher scan rate. It could be seen that the proportion of the capacitive effect was positively related with the scan rates, and it even reached as high as 86.7% at a high scan rate of 50 mV·s^{-1}. Compared with C-CNFs/$NiCo_2O_4$ nanoflake arrays, all the capacitive contribution ratios of P-CNFs/$NiCo_2O_4$ nanoflake arrays at various scan rates were less than that of them (Fig. S12, cf. ESM), suggesting that C-CNFs/$NiCo_2O_4$ nanoflake arrays possessed fast reactions kinetics process. Such fast charge/discharge mechanisms were ascribed to ultrathin nanosheets of $NiCo_2O_4$ and continuous conductive net-

work structure of C-CNFs with high specific surface areas, which provided more electrochemical active contact area with electrolyte. Additionally, the capacitive contributions, CV curves and *b*-value at various scan rates ranging from 1 to 5 $mV \cdot s^{-1}$ were also displayed in Fig. S13 (cf. ESM). A pair of well-defined redox peaks within –0.1 to 0.6 V was clearly observed (Fig. S13(a)), which was consistent with the results of Fig. 5(a). The calculated *b*-values were 0.98 (anodic peaks) and 0.92 (cathodic peaks), and the proportion of the capacitive effect was positively related with the scan rates and it can reach as high as 68.1% at 5 $mV \cdot s^{-1}$ (Figs. S13(b) and S13(c)), further confirming that zinc energy storage mechanism in C-CNFs/$NiCo_2O_4$ nanoflake arrays was capacitance-controlled during the charging/discharging process.

To further confirm the fast ion transport kinetics, the linear relationship of peak current (i_p) and square root of scan rate ($v^{1/2}$) is shown in Fig. 5(f), and the ion diffusion coefficient (*D*) could be calculated based on the Randles-Sevcik equation [39,40]:

$$i_p = \left(2.69 \times 10^5\right) n^{3/2} \times S \times D^{1/2} \times C \times v^{1/2}. \quad (9)$$

Therein, *n* is the number of electrons per molecule attending the electronic transfer reaction, *S* is the area of the electrodes, *C* is the concentration of ion in the electrodes. Obviously, the ion diffusion coefficient of C-CNFs/$NiCo_2O_4$ electrodes (1.33×10^{-9} $cm^2 \cdot s^{-1}$ for anode and 9.64×10^{-10} $cm^2 \cdot s^{-1}$ for cathode) is much higher than the P-CNFs/$NiCo_2O_4$ (2.44×10^{-11} $cm^2 \cdot s^{-1}$ for anode and 4.35×10^{-11} $cm^2 \cdot s^{-1}$ for cathode), proving that the higher ion diffusion kinetics of C-CNFs/$NiCo_2O_4$ nanoflake arrays, which may benefit from the higher effective contact area between high-density ultrathin $NiCo_2O_4$ nanoflake arrays anchored on C-CNFs and electrolyte. And this result is beneficial to the superior high-rate cycling stability.

To quantify the capacitive performance of various electrodes, the GCD curves were carried out at 1–10 $A \cdot g^{-1}$ in Figs. 6, S14 and S15 (cf. ESM). Obviously, all the GCD curves had obvious charging and discharging platform in Figs. 6(a) and 6(b), S14(a) and S15(a), meaning that the Faradaic redox reactions, which corresponded to CV results. The C-CNFs/$NiCo_2O_4$ nanoflake arrays showed a long discharge time (Fig. 6(b)) and a high specific capacitance of 1010 $F \cdot g^{-1}$ at 1 $A \cdot g^{-1}$, which was larger than those capacitances of P-CNFs/$NiCo_2O_4$ nanoflake arrays (976 $F \cdot g^{-1}$, Fig. 6(c)) and bare $NiCo_2O_4$ (966.7 $F \cdot g^{-1}$, Fig. S15(b)). Meanwhile, even at a high current density of 10 $A \cdot g^{-1}$, the specific capacitance of C-CNFs/$NiCo_2O_4$ nanoflake arrays still maintained 666.7 $F \cdot g^{-1}$. Moreover, the electrochemical performance of bare C-CNFs was also illustrated in Fig. S16 (cf. ESM), it showed a small specific capacitance of 174.4 $F \cdot g^{-1}$ at 1 $A \cdot g^{-1}$, only accounting for 17.3% of the specific capacitance of the C-CNFs/$NiCo_2O_4$ nanoflake arrays. Consequently, the $NiCo_2O_4$ contributed most of the specific capacity in composite electrodes instead of C-CNFs as a good conductive carbon matrix. From Fig. 6(d), the long-term stability of C-CNFs/$NiCo_2O_4$ and P-CNFs/$NiCo_2O_4$ nanoflake arrays was established, and the retention of capacitance

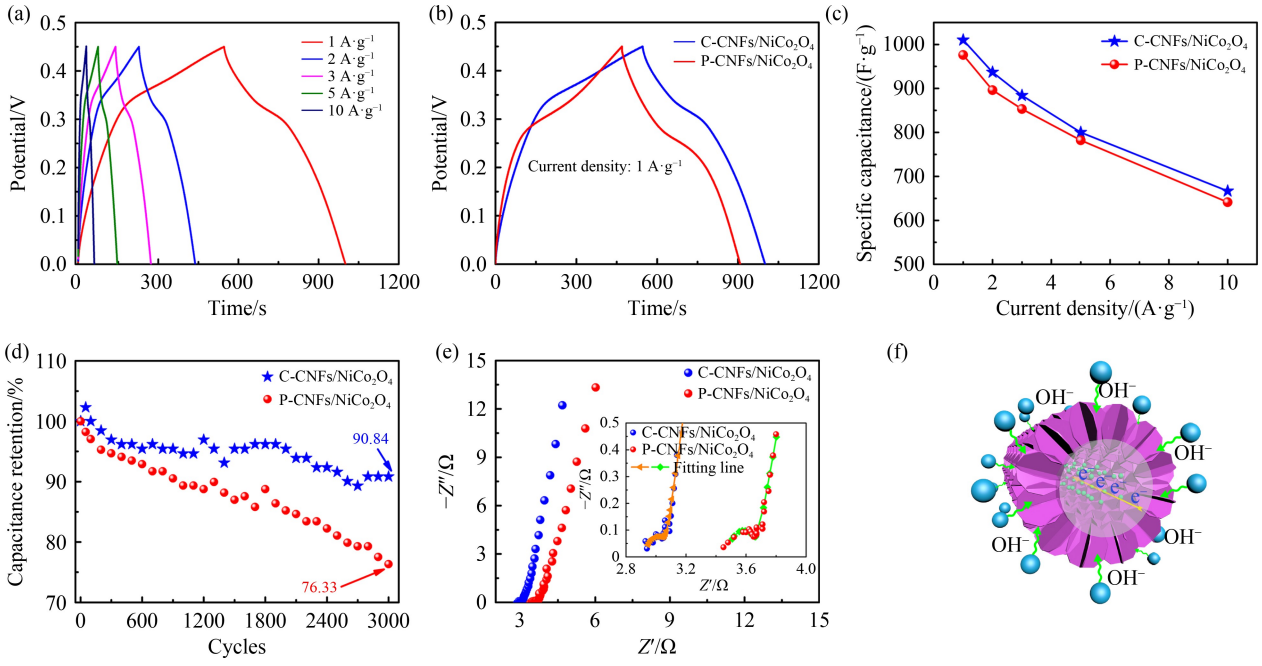

Fig. 6 (a) The GCD curves of C-CNFs/$NiCo_2O_4$ nanoflake arrays at various current densities; (b) the comparison of GCD curves at a current density of 1 $A \cdot g^{-1}$; (c) specific capacitance at various current densities; (d) long-cycling performances and (e) Nyquist plots of C-CNFs/$NiCo_2O_4$ and P-CNFs/$NiCo_2O_4$ nanoflake arrays (inset were the Nyquist plots fitted and the equivalent circuit diagram); (f) the schematic of ion and electron transfer of C-CNFs/$NiCo_2O_4$ nanoflake arrays.

was 90.84% and 76.33% at 10 A·g^{-1} after 3000 cycles, respectively. However, the capacitance retention of bare $NiCo_2O_4$ was only 56.4% at 10 A·g^{-1} after 1000 cycles in Fig. S15(c). The results revealed that the C-CNFs/$NiCo_2O_4$ electrodes had best cycling stability in all electrode materials. The reason of results might be that both high conductivity and specific surface area of C-CNFs were larger than that value of P-CNFs. On one hand, compared with P-CNFs, such high capacity was due to a larger mass of $NiCo_2O_4$ nanoflake arrays anchoring to the C-CNFs; on the other hand, high conductivity of electrodes could accelerate the rapid transfer of electrons and specific surface area of electrodes with multiple mesopores also could promote the permeation and reservoir of the electrolyte ions, which could improve capacity and ensure stable cycles during the fast charging/discharging process [22].

To further study the transport kinetics of the electrochemical reaction process of electrode materials, the EIS test was conducted at open circuit potential in the frequency range between 0.01 Hz and 100 kHz. As shown in Fig. 6(e), the curves were divided into two parts: a semicircle in the high-frequency region and a straight line in the low-frequency area [41]. From the inset of Fig. 6(e), Nyquist plots fitted were carried out by the equivalent circuit (Fig. S17, cf. ESM) for C-CNFs/$NiCo_2O_4$ and P-CNFs/$NiCo_2O_4$ nanoflake arrays. The R_s was regarded as internal resistance and R_{ct} represented the charge transfer resistance at high-frequency region. Compared with the P-CNFs/$NiCo_2O_4$ nanoflake arrays (R_s: 3.48 Ω and R_{ct}: 0.2 Ω), the C-CNFs/$NiCo_2O_4$ nanoflake arrays showed smaller values of R_s (2.93 Ω) and R_{ct} (0.14 Ω), which was beneficial with electrochemical performance owing to fast ion diffusion under low resistance. Moreover, the W_0 was in accordance with Warburg impedance, depending on the kinetics of ion diffusion. Therefore, the value of ion diffusion coefficient was calculated based on the Warburg equation [42]. The ion diffusion coefficient value was 3.45 × 10^{-10} cm^2·s^{-1} (C-CNFs/$NiCo_2O_4$ nanoflake arrays), which was also higher than the value of 8.75 × 10^{-11} cm^2·s^{-1} (P-CNFs/$NiCo_2O_4$ nanoflake arrays), ensuring the fast transfer and diffusion of ion in C-CNFs/$NiCo_2O_4$ nanoflake arrays. In addition, to analyze the ion and electron transfer process of C-CNFs/$NiCo_2O_4$ nanoflake arrays, the schematic diagram of mechanism was illustrated in Fig. 6(f). The C-CNFs was used as current collector to transfer electrons, the effective contact between nanoflake arrays $NiCo_2O_4$ and electrolyte could be used to transport ions (OH^-). The unique 3D nanofiber networks structure of C-CNFs/$NiCo_2O_4$ nanoflake arrays could effectively improve the electric contact between the C-CNFs and the $NiCo_2O_4$, enhancing the electrochemical performance of C-CNFs/$NiCo_2O_4$ nanoflake arrays.

To explore the practical application of C-CNFs/$NiCo_2O_4$ nanoflake arrays electrodes, the ASSCs were fabricated by using two pieces of C-CNFs/$NiCo_2O_4$ electrodes (2 cm × 1 cm) and all the electrochemical performances were displayed in Fig. 7. As shown in Fig. 7(a), the CV curves of ASSCs were performed at 50 mV·s^{-1} between 0.6 and 1.35 V, while the CV shape

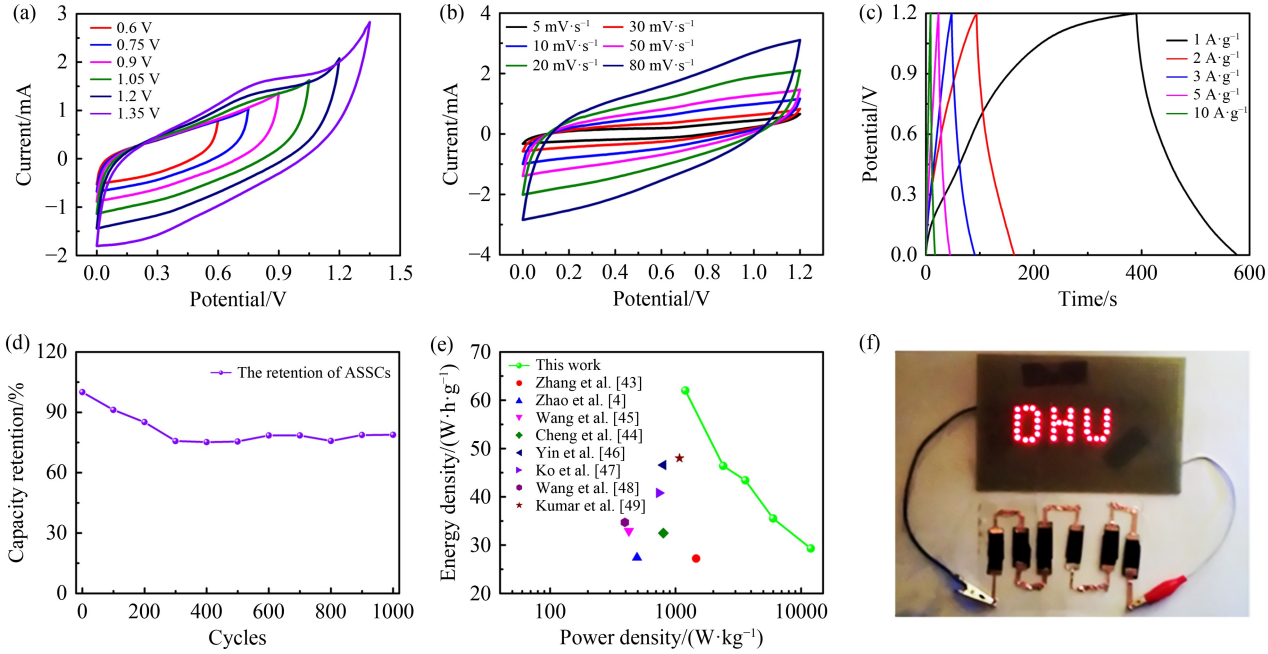

Fig. 7 (a) CV curves of ASSCs with different operating voltages at 50 mV·s^{-1}; (b) CV curves of ASSCs at different scanning rates from 5 to 80 mV·s^{-1}; (c) GCD profiles of ASSCs at various current densities from 1 to 10 A·g^{-1}; (d) cycling performance of ASSCs at 5 A·g^{-1}; (e) Ragone plot of ASSCs our work in comparison with other reported ones; (f) the photographs LED of "DHU" logo on a breadboard powered by ASSCs devices.

of ASSCs deformed due to the serious polarization at a voltage widow of 1.35 V. Thus, the optimized operating voltage of ASSCs was 1.2 V. In addition, the CV curves of ASSCs were analyzed at various scan rates (from 5 to 80 $mV \cdot s^{-1}$) within 0–1.2 V (Fig. 7(b)). The symmetry and rectangular shape of CV curves still could be maintained even at a high scanning rate of 80 $mV \cdot s^{-1}$, confirming good rate performance and reversibility of the assembled ASSCs. From Fig. 7(c), the GCD profiles of ASSCs under various current densities from 1 to 10 $A \cdot g^{-1}$, showed that the specific capacitances were 310.2, 232, 217, 177.5 and 146.7 $F \cdot g^{-1}$ according to Eq. (2), respectively. The cycling performance of ASSCs was displayed in Fig. 7(d), and it maintained the retention of 78.8% at 5 $A \cdot g^{-1}$ after 1000 cycles. Figure 7(e) represented the Ragone plot of ASSCs device in comparison with previous works based on Eqs. (3) and (4) from the GCD curves. The obtained ASSCs device exhibited a maximum energy density of 62 $W \cdot h \cdot kg^{-1}$ at a power density of 1200 $W \cdot kg^{-1}$, which were much larger than previously reported $NiCo_2O_4$ materials [4,43–49]. Moreover, the 'DHU' logo consisted of 36 LEDs could be lighted from six ASSCs devices in series (Fig. 7(f)), suggesting the application potential of electrodes in energy storage.

4 Conclusions

In summary, a novel matrix material of C-CNFs is successfully prepared by a special design of electrospinning, subsequent pre-oxidation and carbonization process. Then both C-CNFs/$NiCo_2O_4$ and P-CNFs/$NiCo_2O_4$ nanoflake arrays are synthesized via a simple one-step solvothermal and calcination method. The electrochemical test results depict that C-CNFs/$NiCo_2O_4$ possesses a better cycling stability (90.84% capacitance retention) than that of P-CNFs/$NiCo_2O_4$ electrodes (76.33% capacitance retention) at a high current density of 10 $A \cdot g^{-1}$ after 3000 cycles, suggesting the superiority of C-CNFs as a substrate in comparison with P-CNFs. The as-prepared ASSCs devices assembled from C-CNFs/$NiCo_2O_4$ can imply a large energy density of 62 $W \cdot h \cdot kg^{-1}$ at a power density of 1200 $W \cdot kg^{-1}$, and six ASSCs in series can power a 'DHU' logo consisting of 36 LEDs, demonstrating the potential application of as-fabricated C-CNFs/$NiCo_2O_4$ electrodes in energy storage systems.

Acknowledgements This work was supported by Key Support Project of State Key Laboratory for Modification of Chemical Fibers and Polymer Materials (Grant No. 21M1060212), Open Project of Shanghai Key Laboratory of Lightweight Structural Composite Materials (Grant No. 2232019A4-02), National Natural Science Foundation of China (Grant No. 51503086) and the Fundamental Research Funds for the Central Universities and Graduate Student Innovation Fund of Donghua University (Grant No. CUSF-DH-D-2022013).

Electronic Supplementary Material Supplementary material is available in the online version of this article at https://dx.doi.org/10.1007/s11705-022-2268-6 and is accessible for authorized users.

References

1. Sun M, Tie J, Cheng G, Lin T, Peng S, Deng F, Ye F, Yu L. In situ growth of burl-like nickel cobalt sulfide on carbon fibers as high-performance supercapacitors. Journal of Materials Chemistry A: Materials for Energy and Sustainability, 2015, 3(4): 1730–1736
2. Han X, Chen Q, Zhang H, Ni Y, Zhang L. Template synthesis of $NiCo_2S_4/Co_9S_8$ hollow spheres for high-performance asymmetric supercapacitors. Chemical Engineering Journal, 2019, 368: 513–524
3. Wu X, Han Z, Zheng X, Yao S, Yang X, Zhai T. Core-shell structured Co_3O_4@$NiCo_2O_4$ electrodes grown on flexible carbon fibers with superior electrochemical properties. Nano Energy, 2017, 31: 410–417
4. Zhao D, Hu F, Umar A, Wu X. $NiCo_2O_4$ nanowire based flexible electrode materials for asymmetric supercapacitors. New Journal of Chemistry, 2018, 42(9): 7399–7406
5. Deng L, Young R J, Kinloch I A, Abdelkader A M, Holmes S M, De Haro-Del Rio D A, Eichhorn S J. Supercapacitance from cellulose and carbon nanotube nanocomposite fibers. ACS Applied Materials & Interfaces, 2013, 5(20): 9983–9990
6. El-Kady M F, Shao Y, Kaner R B. Graphene for batteries, supercapacitors and beyond. Nature Reviews Materials, 2016, 1(7): 1–14
7. Yin J, Zhang W, Alhebshi N A, Salah N, Alshareef H N. Synthesis strategies of porous carbon for supercapacitor applications. Small Methods, 2020, 4(3): 1900853
8. Zhang Z, Bao F, Zhang Y, Feng L, Ji Y, Zhang H, Sun Q, Feng S, Zhao X, Liu X. Formation of hierarchical $CoMoO_4$@MnO_2 core–shell nanosheet arrays on nickel foam with markedly enhanced pseudocapacitive properties. Journal of Power Sources, 2015, 296: 162–168
9. Zhang P, Zhou J, Chen W, Zhao Y, Mu X, Zhang Z, Pan X, Xie E. Constructing highly-efficient electron transport channels in the 3D electrode materials for high-rate supercapacitors: the case of $NiCo_2O_4$@$NiMoO_4$ hierarchical nanostructures. Chemical Engineering Journal, 2017, 307: 687–695
10. Dang A, Sun Y, Liu Y, Xia Y, Liu X, Gao Y, Wu S, Li T, Zada A, Ye F. Flexible $Ti_3C_2T_x$/carbon nanotubes/CuS film electrodes based on a dual-structural design for high-performance all-solid-state supercapacitors. ACS Applied Energy Materials, 2022, 5(7): 9158–9172
11. Li Y, An F, Wu H, Zhu S, Lin C, Xia M, Xue K, Zhang D, Lian K A. $NiCo_2S_4$/hierarchical porous carbon for high performance asymmetrical supercapacitor. Journal of Power Sources, 2019, 427: 138–144
12. Kumar K S, Choudhary N, Jung Y, Thomas J. Recent advances in two-dimensional nanomaterials for supercapacitor electrode applications. ACS Energy Letters, 2018, 3(2): 482–495
13. Wan L, Wang Y, Zhang Y, Du C, Chen J, Tian Z, Xie M. FeCoP nanosheets@Ni-Co carbonate hydroxide nanoneedles as free-

standing electrode material for hybrid supercapacitors. Chemical Engineering Journal, 2021, 415: 128995
14. Zhou Q, Fan T, Li Y, Chen D, Liu S, Li X. Hollow-structure NiCo hydroxide/carbon nanotube composite for high-performance supercapacitors. Journal of Power Sources, 2019, 426: 111–115
15. Shi Z, Shen X, Zhang Z, Wang X, Gao N, Xu Z, Chen X, Liu X. Hierarchically urchin-like hollow $NiCo_2S_4$ prepared by a facile template-free method for high-performance supercapacitors. Journal of Colloid and Interface Science, 2021, 604: 292–300
16. Kunwar R, Krishnan S G, Misnon I I, Zabihi F, Yang S, Yang C C, Jose R. Transformation of supercapacitive charge storage behaviour in a multi-elemental spinel $CuMn_2O_4$ nanofibers with alkaline and neutral electrolytes. Advanced Fiber Materials, 2021, 3(4): 265–274
17. Cai J, Niu H, Li Z, Du Y, Cizek P, Xie Z, Xiong H, Lin T. High-performance supercapacitor electrode materials from cellulose-derived carbon nanofibers. ACS Applied Materials & Interfaces, 2015, 7(27): 14946–14953
18. Cai J, Niu H, Wang H, Shao H, Fang J, He J, Xiong H, Ma C, Lin T. High-performance supercapacitor electrode from cellulose-derived, inter-bonded carbon nanofibers. Journal of Power Sources, 2016, 324: 302–308
19. Frenot A, Henriksson M W, Walkenström P. Electrospinning of cellulose-based nanofibers. Journal of Applied Polymer Science, 2007, 103(3): 1473–1482
20. Kuzmenko V, Naboka O, Gatenholm P, Enoksson P. Ammonium chloride promoted synthesis of carbon nanofibers from electrospun cellulose acetate. Carbon, 2014, 67: 694–703
21. Bhagwan J, Nagaraju G, Ramulu B, Sekhar S C, Yu J S. Rapid synthesis of hexagonal $NiCo_2O_4$ nanostructures for high-performance asymmetric supercapacitors. Electrochimica Acta, 2019, 299: 509–517
22. BoopathiRaja R, Parthibavarman M. Desert rose like heterostructure of $NiCo_2O_4$/NF@PPy composite has high stability and excellent electrochemical performance for asymmetric super capacitor application. Electrochimica Acta, 2020, 346: 136270
23. Wei S, Wan C, Zhang L, Liu X, Tian W, Su J, Cheng W, Wu Y. N-doped and oxygen vacancy-rich $NiCo_2O_4$ nanograss for supercapacitor electrode. Chemical Engineering Journal, 2022, 429: 132242
24. Wang S, Li L, He W, Shao Y, Li Y, Wu Y, Hao X. Oxygen vacancy modulation of bimetallic oxynitride anodes toward advanced Li-ion capacitors. Advanced Functional Materials, 2020, 30(27): 2000350
25. Ni X, Chen H, Liu C, Zeng F, Yu H, Ju A. A freestanding nitrogen-doped carbon nanofiber/MoS_2 nanoflowers with expanded interlayer for long cycle-life lithium-ion batteries. Journal of Alloys and Compounds, 2020, 818: 152835
26. Altin Y, Celik Bedeloglu A. Polyacrylonitrile/polyvinyl alcohol-based porous carbon nanofiber electrodes for supercapacitor applications. International Journal of Energy Research, 2021, 45(11): 16497–16510
27. Hanna S, Yehia A, Ismail M, Khalaf A. Preparation and characterization of carbon fibers from polyacrylonitrile precursors. Journal of Applied Polymer Science, 2012, 123(4): 2074–2083
28. Ni X, Jiang Y, Chen H, Li K, Chen H, Wu Q, Ju A. Fabrication of 3D ordered needle-like polyaniline@hollow carbon nanofibers composites for flexible supercapacitors. Chinese Chemical Letters, 2021, 32(8): 2448–2452
29. Zhang Z, Li L, Qing Y, Lu X, Wu Y, Yan N, Yang W. Manipulation of nanoplate structures in carbonized cellulose nanofibril aerogel for high-performance supercapacitor. Journal of Physical Chemistry C, 2019, 123(38): 23374–23381
30. Wang Y, Ren H, Cheng C, Xu C, Fan G, Liu Y. Tailorable negative permittivity of carbon materials derived from microcrystalline cellulose at different carbonizing temperature. ECS Journal of Solid State Science and Technology, 2020, 9(8): 083001
31. Qiu B, Wang Y, Sun D, Wang Q, Zhang X, Weeks B L, O' Connor R, Huang X, Wei S, Guo Z. Cr(VI) removal by magnetic carbon nanocomposites derived from cellulose at different carbonization temperatures. Journal of Materials Chemistry A: Materials for Energy and Sustainability, 2015, 3(18): 9817–9825
32. Ni X, Cui Z, Luo H, Chen H, Liu C, Wu Q, Ju A. Hollow multi-nanochannel carbon nanofibers@$MoSe_2$ nanosheets composite as flexible anodes for high performance lithium-ion batteries. Chemical Engineering Journal, 2021, 404: 126249
33. Zhang X, Yang F, Chen H, Wang K, Chen J, Wang Y, Song S. In situ growth of 2D ultrathin $NiCo_2O_4$ nanosheet arrays on Ni foam for high performance and flexible solid-state supercapacitors. Small, 2020, 16(44): 2004188
34. Yin X, Li H, Yuan R, Lu J. Metal-organic framework derived hierarchical $NiCo_2O_4$ triangle nanosheet arrays@SiC nanowires network/carbon cloth for flexible hybrid supercapacitors. Journal of Materials Science and Technology, 2021, 81: 162–174
35. Lei D, Li X D, Seo M K, Khil M S, Kim H Y, Kim B S. $NiCo_2O_4$ nanostructure-decorated PAN/lignin based carbon nanofiber electrodes with excellent cyclability for flexible hybrid supercapacitors. Polymer, 2017, 132: 31–40
36. Deng F, Yu L, Cheng G, Lin T, Sun M, Ye F, Li Y. Synthesis of ultrathin mesoporous $NiCo_2O_4$ nanosheets on carbon fiber paper as integrated high-performance electrodes for supercapacitors. Journal of Power Sources, 2014, 251: 202–207
37. Liu C, Jiang W, Hu F, Wu X, Xue D. Mesoporous $NiCo_2O_4$ nanoneedle arrays as supercapacitor electrode materials with excellent cycling stabilities. Inorganic Chemistry Frontiers, 2018, 5(4): 835–843
38. Ni X, Cui Z, Jiang N, Chen H, Wu Q, Ju A, Zhu M. Hollow multi-nanochannel carbon nanofiber/MoS_2 nanoflower composites as binder-free lithium-ion battery anodes with high capacity and ultralong-cycle life at large current density. Journal of Materials Science and Technology, 2021, 77: 169–177
39. Tang S B, Lai M O, Lu L. Li-ion diffusion in highly (003) oriented $LiCoO_2$ thin film cathode prepared by pulsed laser deposition. Journal of Alloys and Compounds, 2008, 449(1): 300–303
40. Rui X H, Yesibolati N, Li S R, Yuan C C, Chen C H. Determination of the chemical diffusion coefficient of Li^+ in intercalation-type $Li_3V_2(PO_4)_3$ anode material. Solid State Ionics, 2011, 187(1): 58–63

41. Khan A S, Pan L, Farid A, Javid M, Huang H, Zhao Y. Carbon nanocoils decorated with a porous $NiCo_2O_4$ nanosheet array as a highly efficient electrode for supercapacitors. Nanoscale, 2021, 13(27): 11943–11952
42. Zhao X, Jia W, Wu X, Lv Y, Qiu J, Guo J, Wang X, Jia D, Yan J, Wu D. Ultrafine MoO_3 anchored in coal-based carbon nanofibers as anode for advanced lithium-ion batteries. Carbon, 2020, 156: 445–452
43. Zhang J N, Liu P, Jin C, Jin L N, Bian S W, Zhu Q, Wang B. Flexible three-dimensional carbon cloth/carbon fibers/$NiCo_2O_4$ composite electrode materials for high-performance all-solid-state electrochemical capacitors. Electrochimica Acta, 2017, 256: 90–99
44. Cheng J P, Wang B Q, Gong S H, Wang X C, Sun Q S, Liu F. Conformal coatings of $NiCo_2O_4$ nanoparticles and nanosheets on carbon nanotubes for supercapacitor electrodes. Ceramics International, 2021, 47(23): 32727–32735
45. Wang W D, Li X F, Zhang P P, Wang B Q, Gong S H, Wang X C, Liu F, Cheng J P. Preparation of $NiCo_2O_4$@CoS heterojunction composite as electrodes for high-performance supercapacitors. Journal of Electroanalytical Chemistry, 2021, 891: 115257
46. Yin X, Li H, Yuan R, Lu J. Hierarchical self-supporting sugar gourd-shape MOF-derived $NiCo_2O_4$ hollow nanocages@SiC nanowires for high-performance flexible hybrid supercapacitors. Journal of Colloid and Interface Science, 2021, 586: 219–232
47. Ko T H, Lei D, Balasubramaniam S, Seo M K, Chung Y S, Kim H Y, Kim B S. Polypyrrole-decorated hierarchical $NiCo_2O_4$ nanoneedles/carbon fiber papers for flexible high-performance supercapacitor applications. Electrochimica Acta, 2017, 247: 524–534
48. Wang L, Jiao X Y, Liu P, Ouyang Y, Xia X F, Lei W, Hao Q L. Self-template synthesis of yolk-shelled $NiCo_2O_4$ spheres for enhanced hybrid supercapacitors. Applied Surface Science, 2018, 427: 174–181
49. Kumar D R, Prakasha K R, Prakash A S, Shim J J. Direct growth of honeycomb-like $NiCo_2O_4$@Ni foam electrode for pouch-type high-performance asymmetric supercapacitor. Journal of Alloys and Compounds, 2020, 836: 155370